INTERNATIONAL JOURNAL FOR NUMERICAL METHODS IN FLUIDS
Int. J. Numer. Meth. Fluids 2006; **51**:305–330
Published online 24 November 2005 in Wiley InterScience (www.interscience.wiley.com). DOI: 10.1002/fld.1126

A simulation of free surface waves for incompressible two-phase flows using a curvilinear level set formulation

W. G. Price[‡] and Y. G. Chen[*,†]

School of Engineering Sciences, Ship Science, University of Southampton, Southampton SO17 1BJ, U.K.

SUMMARY

A level set formulation in a generalized curvilinear coordinate is developed to simulate the free surface waves generated by moving bodies or the sloshing of fluid in a container. The Reynolds-averaged Navier–Stokes (RANS) equations are modified to account for variable density and viscosity in two-phase (i.e. water–air) fluid flow systems. A local level set method is used to update the level set function and a least square technique adopted to re-initialize it at each time step. To assess the developed algorithm and its versatility, a selection of different fluid–structure interaction problems are examined, i.e. an oscillating flow in a two-dimensional square tank, a breaking dam involving different density fluids, sloshing in a two-dimensional rectangular tank and a Wigley ship hull travelling in calm water. Copyright © 2005 John Wiley & Sons, Ltd.

KEY WORDS: level set method; free surface flows; artificial compressibility method; sloshing; broken dam; ship waves

1. INTRODUCTION

The numerical simulation of free surface flows remains a challenging problem in fluid mechanics with applications ranging from ship hydrodynamics to manufacturing processes. The flow around ships and surface piercing marine structures is influenced by free surface phenomena and these fluid–structure interaction systems are governed by a continuity equation, an incompressibility or compressible condition, and Navier–Stokes (N–S) equations. For these kinds of flow interactions, theoretical studies rely on numerical simulations and comparisons with experimental observations because examples described by analytical solutions are not generally available unless the problem is so simplified to be of no merit practically.

*Correspondence to: Y. G. Chen, School of Engineering Sciences, Ship Science, University of Southampton, Southampton SO17 1BJ, U.K.
†E-mail: y.g.chen@ship.soton.ac.uk
‡E-mail: w.g.price@ship.soton.ac.uk

Contract/grant sponsor: Lloyd's Register University Technology Centre

Received 25 May 2005
Revised 21 September 2005
Accepted 25 September 2005

A typical free surface–structure interaction problem includes strong nonlinearity and moving boundaries associated with discontinuities caused by breaking waves and fluid–solid separation. To treat moving boundaries in the solution of nonlinear Navier–Stokes equations, two distinct approaches exist. That is, in interface-tracking methods [1, 2] a moving boundary with its shape and position at any time is determined using kinematic and dynamic boundary conditions and by using different moving and updating grid technologies, such as the arbitrary Lagrangian–Eulerian (ALE) technique, the method deforms the numerical grid to fit the shape of the moving boundaries. The advantage of this approach lies in the fact that it uses a small number of nodes to represent the moving interface and it avoids numerical diffusion which smoothes out the interface. However, when the interface undergoes large deformations with breaking or overturning waves and discontinuities on moving boundaries, the regeneration of meshes becomes difficult.

In the alternative interface-capturing methods [3–18], a fixed computation grid in space is employed and the moving boundaries are captured by solving an additional transport equation on the interfaces. The predefined fixed grid does not move with the moving boundaries which are required to intersect the fixed grid until completion of the calculation. The two most used techniques adopted in the fixed grid method are the marker and cell (MAC) method [3] and the volume of fluid (VOF) method. In the former Lagrangian marker particles are used to identity each fluid, or in modified approaches as described by the SUMMAC and TUMMAC methods [4, 5], where Eulerian markers are used to indicate the interface. In the VOF method [6–9], the average value of the step function defines the volume fraction of one fluid in a cell and the slope of the interface is determined by the gradient of the step function. The major advantages of these methods are their robustness in dealing with problems containing complicated boundary geometries and their relative ease of programming. The main difficulties arising in using these methods are the maintenance of a sharp boundary between the different fluids and the treatment of boundary conditions on curved surfaces. The application of these approaches becomes problematical when details of the surface such as slope and curvature associated with viscous stresses or surface tension are important.

The level set method was developed by Osher and Sethian [10] and has been applied to a wide range of problems such as crystal growth and denditric solidification [11], air bubbles rising in water and water drops falling in air [12], bubbles merging [13], mould filling and the spreading and solidification of molten droplets on a cold substrate [14] and free surface waves [15–18], etc. A level set function, formulated adopting a signed distance function defined on the entire physical domain, is typically a smooth function and the boundary of a two-fluid interface is modelled as the zero set of this function. The boundary is then updated by solving a nonlinear equation of the Hamilton–Jacobi type on the whole domain. This method eliminates the excessive numerical diffusion occurring in conventional numerical difference schemes which destroys the sharpness of the interface and automatically takes care of merging and breaking of the interface. Furthermore, no complexities are added when the method is extended to three dimensions. The level set technique can be considered as an interface capturing technique since no explicit information about the interface is required in the solution procedure. It has the potential to simulate overturning, breaking, merging and reconnection of waves without special treatment.

The computations of free surface viscous flows around ships have been undertaken using moving grid, MAC or VOF methods [1, 2]. The level set method was devised as a versatile and useful tool to analyse the motion of fronts. It has proved to be successful as both a

theoretical and computational device. This study applies the level set technique to simulate free surface waves generated by a marine vehicle [17, 18] moving at the interface of two different fluids or the sloshing of fluid in a container. The RANS equations are modified to account for variable density and viscosity in the two-phase fluid flows.

2. MATHEMATICAL MODEL

2.1. Governing equations

The fluid flow behaviour of an incompressible, immiscible two-fluid system are described by Navier–Stokes equations expressible as

$$\frac{\partial u_j}{\partial x_j} = 0 \tag{1}$$

$$\rho \frac{\partial u_i}{\partial t} = -\frac{\partial}{\partial x_j}(\delta_{ij} p) - \rho \frac{\partial}{\partial x_j}(u_i u_j) + \frac{\partial}{\partial x_j}\left[2 s_{ij}\left(\frac{1}{Re}\mu + \rho \nu_t\right)\right] - \frac{\rho g_i}{Fn^2} - \rho f_i \tag{2}$$

where subscript $i = 1, 2$ or $i = 1, 2, 3$ denotes two- or three-dimensional geometrical descriptions, and a conventional Cartesian tensor notation is used. The coordinates x_i, velocity components u_i and accelerations g_i are non-dimensionalized for each specific problem in terms of a characteristic length L, a characteristic velocity U_0 and gravitational acceleration g. The fluid density ρ and viscosity μ are non-dimensionalized by the corresponding water parameters ρ_w and μ_w, time t by L/U_0 and pressure p by $\rho_w U_0^2$. The strain rate tensor s_{ij} is defined by

$$s_{ij} = \frac{1}{2}\left(\frac{\partial u_i}{\partial x_j} + \frac{\partial u_j}{\partial x_i}\right) \tag{3}$$

In Equation (2), Re and Fn denote Reynolds and Froude numbers, respectively, and are defined as

$$Re = LU_0/\nu_w, \quad Fn = U_0/\sqrt{Lg} \tag{4}$$

Apart from the gravitational force, external forces f_i include translational and rotational inertia forces and are expressible as

$$f_i = a_i + \varepsilon_{ijk}\frac{\mathrm{d}\omega_j}{\mathrm{d}t} x_k + \varepsilon_{ijk}\varepsilon_{klm}\omega_j \omega_l x_m + 2\varepsilon_{ijk}\omega_j u_k \tag{5}$$

where a_i represents the translational acceleration components, ω_i denotes rotational angular velocity components and ε_{ijk} denotes the Levi–Civita symbol with repeating subscripts indicating summation. The influence of surface tension is neglected in this investigation.

Equation (2) is the Reynolds-averaged form of the Navier–Stokes equation where the instantaneous values of velocity and pressure are substituted by their long-time averaged counterparts. A result of this averaging process is the appearance of the Reynolds stress terms ($\overline{u_i u_j}$). Various levels of modelling are available, most of which involve a number of

assumptions and approximations and require considerable experimental input. To simplify the analysis, the turbulence model assumed herein is the Balwin and Barth one-equation model which has its origins in the κ–ε two-equation formulation [19]. In this one-equation formulation, a turbulent eddy viscosity $v\bar{R}_t = \kappa^2/\varepsilon$ is defined and the turbulence field is coupled to the mean field only through the turbulent eddy viscosity v_t, which appears as a part of an effective viscosity $((1/Re) + v_t)$ in the diffusion term of the Reynolds-averaged Navier–Stokes (RANS) equation. Naturally other turbulence models can be integrated into the study by replacement and through modification to the numerical scheme of study developed.

2.2. Level set description

It is assumed that density and viscosity are purely convected by the fluid velocity, and therefore they are constant on particle paths such that

$$\frac{\partial \rho}{\partial t} + u_j \frac{\partial \rho}{\partial x_j} = 0 \tag{6}$$

$$\frac{\partial \mu}{\partial t} + u_j \frac{\partial \mu}{\partial x_j} = 0 \tag{7}$$

Since density and viscosity are discontinuous at a free surface, conventional finite difference schemes incur excessive numerical diffusion when solving Equations (6) and (7). Instead, we use the level set technique to capture the free surface as described by Sussman *et al.* [12].

The free surface is defined as the zero level set of a level-set function ϕ. The other values of this function have no significance and to make it a smooth function, ϕ is typically initialized as a signed distance function from the interface, i.e. its value at any point is the distance from the nearest point on the interface and its sign is positive on one side and negative on the other. Let us set ϕ as positive in air and negative in water by defining

$$\begin{aligned} \phi(x_i, t) &> 0 \quad \text{in air} \\ \phi(x_i, t) &= 0 \quad \text{on surface} \\ \phi(x_i, t) &< 0 \quad \text{in water} \end{aligned} \tag{8}$$

Differentiating $\phi = 0$ with respect to t allows derivation of the free surface transport equation

$$\frac{\partial \phi}{\partial t} + u_j \frac{\partial \phi}{\partial x_j} = 0 \tag{9}$$

where u_j is the local fluid velocity and, at any time, moving the interface is equivalent to updating ϕ by solving Equation (9). The advantage of this method relative to the VOF method is that ϕ is a smooth function as the density ρ and viscosity μ in Equations (6) and (7) vary across the interface.

Due to the sharp change of fluid properties at the free surface, problems are experienced when computing viscous flows as discussed by Ferziger [20]. We therefore need to introduce a region of finite thickness over which a smooth but rapid change of density and viscosity

occurs across the interface. This is achieved by defining a smoothed Heaviside function $H_\varepsilon(x)$ satisfying

$$H_\varepsilon(x) = \begin{cases} 1 & \text{if } x > \varepsilon \\ 0 & \text{if } x < -\varepsilon \\ 0.5(x+\varepsilon)/\varepsilon + 0.5\sin(\pi x/\varepsilon)/\pi & \text{otherwise} \end{cases} \tag{10}$$

where ε denotes half the finite thickness of the interface in which the density and viscosity change.

Using this smoothed Heaviside function, we can define a corresponding smoothed density function ρ and smoothed viscosity function μ expressed as

$$\rho_\varepsilon(\phi) = 1 + (\rho_a/\rho_w - 1)H_\varepsilon(\phi) \tag{11}$$

$$\mu_\varepsilon(\phi) = 1 + (\mu_a/\mu_w - 1)H_\varepsilon(\phi) \tag{12}$$

3. THE NAVIER–STOKES EQUATION SOLVER FOR TWO PHASE FLOWS

It can be shown that the continuity equation (1) and the momentum equation (2) expressible in a curvilinear coordinate system ($\xi_1 = \xi, \xi_2 = \eta, \xi_3 = \zeta$) are given by

$$\frac{1}{J^{-1}}\,\partial(J^{-1}U_i)\Big/\partial\xi_i = 0 \tag{13}$$

$$\frac{\partial d}{\partial t} = -\frac{\partial(e^i - e_v^i)}{\partial\xi_i} - f \equiv -r \tag{14}$$

where the vector d is defined by

$$d = J^{-1}\rho_\varepsilon \begin{bmatrix} u \\ v \\ w \end{bmatrix} \tag{15}$$

Here $J = \partial(\xi,\eta,\zeta)/\partial(x,y,z)$ is the Jacobian of the transformation, and the convective fluxes, viscous fluxes and the external forces are, respectively, given by

$$e^i = J^{-1}\begin{bmatrix} \rho_\varepsilon u_1 U_i + \dfrac{\partial\xi_i}{\partial x_1}p \\ \rho_\varepsilon u_2 U_i + \dfrac{\partial\xi_i}{\partial x_2}p \\ \rho_\varepsilon u_3 U_i + \dfrac{\partial\xi_i}{\partial x_3}p \end{bmatrix}$$

$$e_v^i = J^{-1}\left(\frac{\mu_\varepsilon}{Re} + \rho_\varepsilon v_t\right)\begin{bmatrix} \dfrac{\partial \xi_i}{\partial x_m}\dfrac{\partial \xi_k}{\partial x_m}\dfrac{\partial u_1}{\partial \xi_k} \\ \dfrac{\partial \xi_i}{\partial x_m}\dfrac{\partial \xi_k}{\partial x_m}\dfrac{\partial u_2}{\partial \xi_k} \\ \dfrac{\partial \xi_i}{\partial x_m}\dfrac{\partial \xi_k}{\partial x_m}\dfrac{\partial u_3}{\partial \xi_k} \end{bmatrix}$$

$$f = J^{-1}\rho_\varepsilon \begin{bmatrix} \dfrac{g_1}{Fn^2} + f_1 \\ \dfrac{g_2}{Fn^2} + f_2 \\ \dfrac{g_3}{Fn^2} + f_3 \end{bmatrix} \tag{16}$$

where the contravariant velocity components U_i are defined by

$$U_i = \frac{\partial \xi_i}{\partial x_m} u_m \tag{17}$$

To construct a numerical scheme of study to solve Equations (13) and (14), an artificial compressibility relation [21, 22] is introduced by adding a virtual time derivative of pressure to the continuity equation modifying Equation (13) to

$$\frac{\partial (p/\beta)}{\partial \tau} = -\frac{1}{J^{-1}}\frac{\partial (J^{-1}U_i)}{\partial \xi_i} \tag{18}$$

where τ indicates the virtual time variable and β denotes the artificial compressibility factor.

The application of an implicit Euler backward difference formulation to approximate the virtual time derivative in Equation (18) and a second-order, three-point, backward-difference implicit formulation to approximate the time derivate in the momentum equation (14), allows the replacement of Equations (18) and (14), respectively, by

$$J^{-1}\frac{p^{n+1,m+1} - p^{n+1,m}}{\beta \partial \tau} = -\left(\frac{\partial (J^{-1}U_i)}{\partial \xi_i}\right)^{n+1,m+1} \tag{19}$$

$$\frac{1.5d^{n+1,m+1} - 1.5d^{n+1,m}}{\Delta t} = -r^{n+1,m+1} - \frac{1.5d^{n+1,m} - 2d^n + 0.5d^{n-1}}{\Delta t} \tag{20}$$

where the first superscript n denotes the physical time step level and second superscript m the level of the sub-iteration used to converge solutions of Equations (13) and (14) for each time step.

Combining Equations (9), (19) and (20), we find that the discretized, incremental equation derived by linearizing the right-hand residual term R at the $(m+1)$th virtual time level is

given by

$$\left[J^{-1}I_{tr}+J^{-1}\left(\frac{\partial R}{\partial D}\right)^{n+1,m}I_{\rho}\right](\tilde{D}^{n+1,m+1}-\tilde{D}^{n+1,m})$$

$$=-R^{n+1,m}-\frac{I_m}{\Delta t}(1.5D^{n+1,m}-2D^n+0.5D^{n-1}) \tag{21}$$

Here I_{tr}, I_m and I_{ρ} represent the three diagonal matrices

$$I_{tr}=\text{diag}\left[\frac{1}{\beta\Delta\tau},\frac{1.5\rho_{\varepsilon}}{\Delta t},\frac{1.5\rho_{\varepsilon}}{\Delta t},\frac{1.5\rho_{\varepsilon}}{\Delta t},\frac{1.5}{\Delta t}\right]$$

$$I_m=\text{diag}[0,1,1,1,1],\quad I_{\rho}=\text{diag}[1/\beta,\rho_{\varepsilon},\rho_{\varepsilon},\rho_{\varepsilon},1] \tag{22}$$

and D, $\tilde{D}$, R, E^i and E^i_v are defined by

$$\tilde{D}=\begin{bmatrix}p\\u\\v\\w\\\phi\end{bmatrix},\quad D=J^{-1}I_{\rho}\tilde{D}$$

$$E^i=\begin{bmatrix}J^{-1}U_i\\e^i\\J^{-1}U_i\phi\end{bmatrix}$$

$$E^i_v=\begin{bmatrix}0\\e^i_v\\0\end{bmatrix}$$

$$R=\partial(E^i-E^i_v)/\partial\xi_i+F \tag{23}$$

where the external force vector F is given by

$$F=\begin{bmatrix}0\\f\\0\end{bmatrix}$$

The derivative of the convective flux E^1 in the ξ direction is approximated at node (j,k,l) by

$$\frac{\partial E^1}{\partial \xi} \approx \frac{\tilde{E}^1_{j+1/2,k,l} - \tilde{E}^1_{j-1/2,k,l}}{\Delta \xi} \tag{24}$$

The numerical flux $\tilde{E}^1_{j+1/2,k,l}$ at the interface $(j+1/2,k,l)$ which separates the cell (j,k,l) and cell $(j+1,k,l)$ is calculated by Roe's approximate Riemann solver [23] and is given by

$$\begin{aligned}\tilde{E}^1_{j+1/2,k,l} = \tfrac{1}{2}\,[&E^1(D^{\mathrm{L}}_{j+1/2,k,l}) + E^1(D^{\mathrm{R}}_{j+1/2,k,l}))\\ &-|A(D^{\mathrm{L}}_{j+1/2,k,l}, D^{\mathrm{R}}_{j+1/2,k,l})|(D^{\mathrm{R}}_{j+1/2,k,l} - D^{\mathrm{L}}_{j+1/2,k,l})]\end{aligned} \tag{25}$$

where the superscripts 'R' and 'L' indicate the right and left states. In this expression A is the Jacobian of the convective flux vector E^1 and $|A| = T|\Lambda|T^{-1}$, where T is the matrix whose columns are the right eigenvectors of A, T^{-1} is the matrix whose rows are the left eigenvectors of A, and $|\Lambda|$ is a diagonal matrix whose elements are the absolute values of the eigenvalues of A. The matrix A, dependent on left and right states $D^{\mathrm{L}}_{j+1/2,k,l}$ and $D^{\mathrm{R}}_{j+1/2,k,l}$ at the interface $(j+1/2,k,l)$, is evaluated using Roe-average variables. In the two-phase fluid system under examination, the appropriate Roe average variables are given by

$$\begin{aligned}\bar{p}^{\mathrm{Roe}} &= (p^{\mathrm{R}} + p^{\mathrm{L}})/2\\ \bar{\mathrm{u}}^{\mathrm{Roe}} &= (\lambda \mathrm{u}^{\mathrm{R}} + \mathrm{u}^{\mathrm{L}})/(1+\lambda)\\ \bar{\mathrm{v}}^{\mathrm{Roe}} &= (\lambda \mathrm{v}^{\mathrm{R}} + \mathrm{v}^{\mathrm{L}})/(1+\lambda)\\ \bar{\mathrm{w}}^{\mathrm{Roe}} &= (\lambda \mathrm{w}^{\mathrm{R}} + \mathrm{w}^{\mathrm{L}})/(1+\lambda)\\ \bar{\phi}^{\mathrm{Roe}} &= (\phi^{\mathrm{R}} + \phi^{\mathrm{L}})/2\\ \bar{\rho}_{\varepsilon}{}^{\mathrm{Roe}} &= \lambda \rho^{\mathrm{L}}_{\varepsilon}\\ \lambda &= \sqrt{\rho^{\mathrm{R}}_{\varepsilon}/\rho^{\mathrm{L}}_{\varepsilon}}\end{aligned} \tag{26}$$

The application of a first-order Roe's approximation, which assumes a piecewise constant profile of D, to the left and right states in Equation (25) gives

$$D^{\mathrm{R}}_{j+1/2,k,l} = D_{j+1,k,l}, D^{\mathrm{L}}_{j+1/2,k,l} = D_{j,k,l} \tag{27}$$

The (5×5) inviscid flux Jacobian matrix A, matrix T and its inverse T^{-1} are written as

$$A = \frac{\partial E^1}{\partial D} = \begin{bmatrix} 0 & \frac{\partial \xi}{\partial x}\Big/\rho_\varepsilon & \frac{\partial \xi}{\partial y}\Big/\rho_\varepsilon & \frac{\partial \xi}{\partial z}\Big/\rho_\varepsilon & 0 \\ \beta\frac{\partial \xi}{\partial x} & \frac{\partial \xi}{\partial x}u + U_1 & \frac{\partial \xi}{\partial y}u & \frac{\partial \xi}{\partial z}u & 0 \\ \beta\frac{\partial \xi}{\partial y} & \frac{\partial \xi}{\partial x}v & \frac{\partial \xi}{\partial y}v + U_1 & \frac{\partial \xi}{\partial z}v & 0 \\ \beta\frac{\partial \xi}{\partial z} & \frac{\partial \xi}{\partial x}w & \frac{\partial \xi}{\partial y}w & \frac{\partial \xi}{\partial z}w + U_1 & 0 \\ 0 & \frac{\partial \xi}{\partial x}\phi\Big/\rho_\varepsilon & \frac{\partial \xi}{\partial y}\phi\Big/\rho_\varepsilon & \frac{\partial \xi}{\partial z}\phi\Big/\rho_\varepsilon & U_1 \end{bmatrix}$$

$$T = \begin{bmatrix} 0 & 0 & c/\rho_\varepsilon & -c/\rho_\varepsilon & 0 \\ \frac{\partial x}{\partial \eta} & \frac{\partial x}{\partial \zeta} & \lambda_3 u + \frac{\partial \xi}{\partial x}\frac{\beta}{\rho_\varepsilon} & \lambda_4 u + \frac{\partial \xi}{\partial x}\frac{\beta}{\rho_\varepsilon} & 0 \\ \frac{\partial y}{\partial \eta} & \frac{\partial y}{\partial \zeta} & \lambda_3 v + \frac{\partial \xi}{\partial y}\frac{\beta}{\rho_\varepsilon} & \lambda_4 v + \frac{\partial \xi}{\partial y}\frac{\beta}{\rho_\varepsilon} & 0 \\ \frac{\partial z}{\partial \eta} & \frac{\partial z}{\partial \zeta} & \lambda_3 w + \frac{\partial \xi}{\partial z}\frac{\beta}{\rho_\varepsilon} & \lambda_4 w + \frac{\partial \xi}{\partial z}\frac{\beta}{\rho_\varepsilon} & 0 \\ 0 & 0 & \frac{\phi}{\rho_\varepsilon}\lambda_3 & \frac{\phi}{\rho_\varepsilon}\lambda_4 & 1 \end{bmatrix}$$

$$T^{-1} = \frac{1}{c^2}\begin{bmatrix} \beta\left(\frac{\partial x}{\partial \zeta}\left(\frac{\partial \xi}{\partial z}v - \frac{\partial \xi}{\partial y}w\right) + \frac{\partial y}{\partial \zeta}\left(\frac{\partial \xi}{\partial x}w - \frac{\partial \xi}{\partial z}u\right) + \frac{\partial z}{\partial \zeta}\left(\frac{\partial \xi}{\partial y}u - \frac{\partial \xi}{\partial x}v\right)\right) \\ \beta\left(\frac{\partial x}{\partial \eta}\left(\frac{\partial \xi}{\partial y}w - \frac{\partial \xi}{\partial z}v\right) + \frac{\partial y}{\partial \eta}\left(\frac{\partial \xi}{\partial z}u - \frac{\partial \xi}{\partial x}w\right) + \frac{\partial z}{\partial \eta}\left(\frac{\partial \xi}{\partial x}v - \frac{\partial \xi}{\partial y}u\right)\right) \\ -0.5\rho_\varepsilon\lambda_4 \\ -0.5\rho_\varepsilon\lambda_3 \\ \lambda_3\lambda_4\phi \end{bmatrix}$$

$$\begin{bmatrix} \frac{\partial y}{\partial \zeta}\left(\lambda_1 w + \beta\frac{\partial \xi}{\partial z}\Big/\rho_\varepsilon\right) - \frac{\partial z}{\partial \zeta}\left(\lambda_1 v + \beta\frac{\partial \xi}{\partial y}\Big/\rho_\varepsilon\right) \\ -\frac{\partial y}{\partial \eta}\left(\lambda_1 w + \beta\frac{\partial \xi}{\partial z}\Big/\rho_\varepsilon\right) + \frac{\partial z}{\partial \eta}\left(\lambda_1 v + \beta\frac{\partial \xi}{\partial y}\Big/\rho_\varepsilon\right) \\ 0.5\frac{\partial \xi}{\partial x} \\ 0.5\frac{\partial \xi}{\partial x} \\ -\lambda_5\phi\frac{\partial \xi}{\partial x}\Big/\rho_\varepsilon \end{bmatrix}$$

$$\begin{bmatrix}
\dfrac{\partial z}{\partial \zeta}\left(\lambda_1 u+\beta\ \dfrac{\partial \xi}{\partial x}\Big/\rho_\varepsilon\right)-\dfrac{\partial x}{\partial \zeta}\left(\lambda_1 w+\beta\dfrac{\partial \xi}{\partial z}\Big/\rho_\varepsilon\right) & \dfrac{\partial x}{\partial \zeta}\left(\lambda_1 v+\beta\dfrac{\partial \xi}{\partial y}\Big/\rho_\varepsilon\right)-\dfrac{\partial y}{\partial \zeta}\left(\lambda_1 u+\beta\dfrac{\partial \xi}{\partial x}\Big/\rho_\varepsilon\right) & 0 \\
-\dfrac{\partial z}{\partial \eta}\left(\lambda_1 u+\beta\dfrac{\partial \xi}{\partial x}\Big/\rho_\varepsilon\right)+\dfrac{\partial x}{\partial \eta}(\lambda_1 w+\beta\dfrac{\partial \xi}{\partial z}\Big/\rho_\varepsilon) & -\dfrac{\partial x}{\partial \eta}\left(\lambda_1 v+\beta\dfrac{\partial \xi}{\partial y}\Big/\rho_\varepsilon\right)+\dfrac{\partial y}{\partial \eta}\left(\lambda_1 u+\beta\dfrac{\partial \xi}{\partial x}\Big/\rho_\varepsilon\right) & 0 \\
0.5\dfrac{\partial \xi}{\partial y} & 0.5\dfrac{\partial \xi}{\partial z} & 0 \\
0.5\dfrac{\partial \xi}{\partial y} & 0.5\dfrac{\partial \xi}{\partial z} & 0 \\
-\lambda_5\phi\dfrac{\partial \xi}{\partial y}\Big/\rho_\varepsilon & -\lambda_5\phi\dfrac{\partial \xi}{\partial z}\Big/\rho_\varepsilon & c^2
\end{bmatrix} \tag{28}$$

Here λ_1, λ_2, λ_3, λ_4 and λ_5 denote the eigenvalues of A, given by

$$\lambda_1=\lambda_2=\lambda_5=U_1,\quad \lambda_3=U_1+c,\quad \lambda_4=U_1-c \tag{29}$$

where

$$c=\sqrt{U_1^2+\frac{\partial \xi}{\partial x_i}\frac{\partial \xi}{\partial x_i}\frac{\beta}{\rho_\varepsilon}}$$

The derivatives of the convective fluxes E^2 in the η direction and E^3 in the ζ direction are derived similarly to the description of E^1.

The derivatives of the viscous fluxes defined in Equation (21) are approximated by using a second-order central difference scheme. Following Equation (23), the residual vector R at node (j,k,l) is approximated by

$$\begin{aligned}
R_{j,k,l}=&\frac{\tilde{E}^1_{j+1/2,k,l}-\tilde{E}^1_{j-1/2,k,l}}{\Delta\xi}+\frac{\tilde{E}^2_{j,k+1/2,l}-\tilde{E}^2_{j,k-1/2,l}}{\Delta\eta}+\frac{\tilde{E}^3_{j,k,l+1/2}-\tilde{E}^3_{j,k,l-1/2}}{\Delta\zeta}\\
&-\frac{(E^1_v)_{j+1,k,l}-(E^1_v)_{j-1,k,l}}{2\Delta\xi}-\frac{(E^2_v)_{j,k+1,l}-(E^2_v)_{j,k-1,l}}{2\Delta\eta}\\
&-\frac{(E^3_v)_{j,k,l+1}-(E^3_v)_{j,k,l-1}}{2\Delta\zeta}-F_{j,k,l}
\end{aligned} \tag{30}$$

Numerical convective fluxes in vector R are discretized by applying a third-order upwind difference scheme to Equation (25). The interested reader may consult Rogers and Kwak [24], Kelecy and Pletcher [25], and Toro [26] for the details describing the implementation of high order schemes.

The computation of Jacobian matrix $\partial R/\partial D$ is very time consuming and difficult if derived exactly in full. Therefore, to simplify the computational process of $\partial R/\partial D$ on the left-hand side of Equation (21), only a first-order difference scheme is applied to the approximation of the numerical convective fluxes and the orthogonal mesh terms are retained to include the viscous terms. The formulation to approximate $\partial R/\partial D$ is derived as follows.

On linearizing the numerical convective flux term $\tilde{E}^1$ at the $(m+1)$th virtual time step, we find that

$$\begin{aligned}(\tilde{E}^1_{j+1/2,k,l})^{m+1} &\approx (\tilde{E}^1_{j+1/2,k,l})^m + \left(\frac{\partial \tilde{E}^1_{j+1/2,k,l}}{\partial \tau}\right)^m \Delta\tau \\ &= (\tilde{E}^1_{j+1/2,k,l})^m + \left(\frac{\partial \tilde{E}^1_{j+1/2,k,l}}{\partial D_{j,k,l}}\right)^m \frac{\partial D_{j,k,l}}{\partial \tau}\Delta\tau \\ &\quad + \left(\frac{\partial \tilde{E}^1_{j+1/2,k,l}}{\partial D_{j+1,k,l}}\right)^m \frac{\partial D_{j+1,k,l}}{\partial \tau}\Delta\tau \end{aligned} \tag{31}$$

where the first superscript n is omitted for simplification. By neglecting the derivative terms of $|A|$ with respect to the left and right states $D_{j,k,l}$ and $D_{j+1,k,l}$ in Equation (25) based on Barth's [27] analysis, the second and third terms on the right-hand side of the previous equation are, respectively, written as

$$\left(\frac{\partial \tilde{E}^1_{j+1/2,k,l}}{\partial D_{j,k,l}}\right)^m \frac{\partial D_{j,k,l}}{\partial \tau}\Delta\tau \approx \frac{1}{2}(A_{j,k,l} + |A_{j+1/2,k,l}|)\Delta D_{j,k,l}$$

and

$$\left(\frac{\partial \tilde{E}^1_{j+1/2,k,l}}{\partial D_{j+1,k,l}}\right)^m \frac{\partial D_{j+1,k,l}}{\partial \tau}\Delta\tau \approx \frac{1}{2}(A_{j+1,k,l} - |A_{j+1/2,k,l}|)\Delta D_{j+1,k,l}$$

where $\Delta D_{j,k,l} = D^{m+1}_{j,k,l} - D^m_{j,k,l}$.

The substitution of these two equations into Equation (31) finally yields

$$\begin{aligned}(\tilde{E}^1_{j+1/2,k,l})^{m+1} &\approx (\tilde{E}^1_{j+1/2,k,l})^m + \tfrac{1}{2}(A_{j,k,l} + |A_{j+1/2,k,l}|)\Delta D_{j,k,l} \\ &\quad + \tfrac{1}{2}(A_{j+1,k,l} - |A_{j+1/2,k,l}|)\Delta D_{j+1,k,l}\end{aligned} \tag{32}$$

The linearization of all the other terms in the residual vector R including the viscous flux vectors and the external force vector are derived similarly to the description of $\tilde{E}^1$.

It is noted that Equation (21) is expressed in an incremental form based on the flow variable difference between iterations $\Delta\tilde{D} = \tilde{D}^{n+1,m+1} - \tilde{D}^{n+1,m}$. Therefore, as long as the solution converges in virtual time (i.e. $\Delta\tilde{D} \to 0$ as $m \to \infty$), the computed solution is not affected by any approximation such as using a one-order upwind difference method to compute the convective fluxes in the Jacobian matrix $\partial R/\partial D$. Meanwhile, since the right-hand side of Equation (21) becomes zero, the computed solution satisfies the original governing equations.

The calculation of Jacobian matrices of convective flux vectors in Equation (25) plays an important role in the stability of the developed algorithm. The normal velocity components and pressure across the interface are continuous, when surface tension effect is neglected, but density values jump across the interface. Therefore, to enhance stability, the incremental term ΔD in the numerical convective fluxes is calculated by

$$\Delta D = \frac{\partial D}{\partial \tilde{D}}(D^{\mathrm{L}}, D^{\mathrm{R}})\Delta\tilde{D}$$

where D, $\tilde{D}$, D^{L} and D^{R} are defined in Equations (23) and (25). That is, $\partial D/\partial\tilde{D}$ is defined as the function of Roe's average variables.

4. LOCALIZATION OF LEVEL SET FORMULATION AND ITS RE-INITIALIZATION

It follows from Equation (9) that knowing ϕ allows location of the interface by finding the zero level set of ϕ. That is, the interface is determined by the local value of ϕ as given by Equation (9). Moreover, only the sign of ϕ is important when locating the interface.

As discussed by Sussman *et al.* [12] and Peng *et al.* [28], even if we initialize ϕ as a signed distance from the front, i.e. free surface, the level set function will no longer remain a distance function at later times. For numerical reasons, we need to re-initialize the level set function so that ϕ satisfies $|\nabla\phi| = 1$. This process is referred to as the distance re-initialization of the level set function. A straightforward approach for re-initialization is to find the location of the zero level set $\phi = 0$ and by interpolation to update ϕ as a signed distance function to this front [15]. This procedure is found effective in retaining mass conservation and is a simple process when dealing with two-dimensional problems, but for three-dimensional problems and complicated interface topologies, it is of high cost and a smoothing procedure is usually needed in addition to the proposed approach [15].

An iterative procedure [12] is used to re-initialize the level set function at each time step by solving the Hamilton–Jacobi equation based on essentially non-oscillatory schemes [29, 30] (ENO) associated with the steady state solution. That is

$$\frac{\partial\varphi}{\partial\tau} = \mathrm{sgn}(\phi_0)(1 - |\nabla\varphi|)$$

$$\varphi(x, 0) = \phi_0(x) \tag{33}$$

where sgn represents the sign function. By specifying the value ϕ_0 of the level set function at time t as an initial condition, the steady-state solution φ of Equation (33) has the same sign and zero level set as ϕ_0, and converges to $|\varphi| = 1$. Therefore, it is a distance function to

the front or free surface. For numerical reasons, this sign function is approximated by [12]

$$S_\varepsilon(\phi_0) = \frac{\phi_0}{\sqrt{\phi_0^2 + \varepsilon^2}} \tag{34}$$

In this investigation, a least square method [31] is adopted to re-initialize the level set function. We derive ϕ by solving Equation (21) within a narrow band of the free surface and re-initialize ϕ in a slightly larger region. For example, when two adjacent points along the coordinate line ξ satisfy the inequality

$$\phi_{j,k,l}\phi_{j+1,k,l} \leqslant 0 \tag{35}$$

we only compute ϕ at a few grid points surrounding the point (j,k,l) according to the order of difference scheme used to solve Equation (21). A blanking technique is implemented in the fluid flow solver to blank out points of no interest so that the level set function ϕ is only updated in a narrow band in the vicinity of the free surface. A switch variable

$$ib(j,k,l) = \begin{cases} 1 & \text{a point inside the narrow band of the free surface} \\ 0 & \text{a point outside the narrow band of the free surface} \end{cases} \tag{36}$$

is introduced to achieve this goal. The procedure developed requires the multiplication by ib to the matrix coefficients on the left-hand side and the vector on the right-hand side of the algebraic equation (21) and through assigning the diagonal terms of the matrix to be unity for those points satisfying $ib = 0$.

5. NUMERICAL RESULTS

In this section, the developed numerical method is applied to a selection of free surface flow problems. That is, (i) an oscillating flow in a two-dimensional square tank which enables the testing of the accuracy of the level set method to capture interface behaviour. It provides a measure of validation of the developed numerical algorithm and an assessment of its capability to preserve mass; (ii) to demonstrate the effect of gravity a broken dam problem is constructed to investigate the resulting flow and free surface characteristics after failure. The influence of the density ratio of the two phase fluid flow, i.e. 1:10, 1:100 and 1:1000 are examined and this selection provides an indication of the versatility of the solution procedure; (iii) a forced motion problem is investigated involving fluid sloshing in a partially filled two-dimensional tank undergoing sinusoidal excitation. The free surface behaviour is assessed for a range of oscillating frequency values and amplitudes of oscillation. This demonstrates the applicability and performance of the level set based algorithm to capture free surface wave disturbances and, if successful, provides a measure of confidence to extend the numerical approach to a three-dimensional sloshing problem in arbitrary shaped tanks; (iv) as part of the process of transition to examine three-dimensional fluid–structure interactions involving free surfaces, the numerical scheme of study is suitably modified to examine the free surface waves generated by a Wigley ship hull travelling at a prescribed Froude number in calm water. Wave profiles are generated together with a selection of pressure and drag coefficient values to assess the refinement of idealization on predicted values. In all these examples and where possible,

either experimental data and/or computational results from other investigations are included for comparison.

There is no special treatment required for the description of the interface as it is treated as an internal boundary of the physical domain due to the two-phase flow model adopted here. The slip or no-slip velocity boundary condition is imposed on the solid walls and the pressure on the walls is obtained by projecting the momentum equation along the normal to the wall. On the top boundary of the computational domain in the air region the velocity components and pressure are both set to zero. Such a treatment of the top pressure boundary condition is reasonable when this boundary is some distance away from the interface and this procedure speeds up the convergence process in the numerical experiments performed. For the ship wave calculations in Section 5.4, extrapolation of physical variables is used for outside and outflow boundaries.

The initial conditions for all proceeding calculations are given as follows. Except for the ship wave simulations where a uniform flow velocity field is specified, the velocity components are set to zero everywhere in the whole computational domain although in the ship simulation this is not valid because of the forward speed of the vessel. In all cases, the initial value of the level set function is set as the signed distance from the interface, positive in the air region and negative in the fluid domain, and the pressure distribution is defined by its hydrostatic value in the fluid below the interface and zero everywhere else.

Theoretically, the artificial compressibility factor β is chosen as large as the numerical algorithm allows so that any disturbance in the flow field is propagated rapidly to the entire flow field including both gas and fluid regions. Compared to a single-phase flow, the factor β in the artificial speed of sound c in Equation (29) is replaced by the corresponding value β/ρ_ε where ρ_ε is a non-dimensional density. Numerical experiments revealed that the convergence of the current scheme is not sensitive to the value of β when of the order of $1\times10^{+4}$–$1\times10^{+6}$. For this reason, the value of β was set to either $1\times10^{+5}$ or $5\times10^{+5}$ for all test cases.

The density and viscosity distributions are smoothed by introducing the smoothed Heaviside function into Equations (11) and (12) so that the density and viscosity values at the interface are defined as $(\rho_a+\rho_w)/2$ and $(\mu_a+\mu_w)/2$, respectively. Unless otherwise mentioned, for all cases, the half thickness of the interface ε is chosen so that the jump in density covers three grid cells in the normal direction to the interface.

In the presented numerical examples, the physical properties chosen are: density of water $\rho_w=998.1\,\mathrm{kg/m^3}$, density of air $\rho_a=1.20\,\mathrm{kg/m^3}$, with corresponding dynamic viscosities $\mu_w=1.0\times10^{-3}\,\mathrm{kg/ms}$ and $\mu_a=1.81\times10^{-5}\,\mathrm{kg/ms}$, respectively. The effect of surface tension is neglected in this investigation.

5.1. Oscillating flow in a two-dimensional tank

Iafrati *et al.* [15] examined an oscillating flow in a tank of unit breadth and depth of water. A similar numerical experiment is presented herein to allow comparison of the predictions derived by the proposed numerical scheme of study and to assess the algorithm's capability to preserve mass. In this example, the tank extends horizontally between $-0.5\leqslant x\leqslant 0.5$ and vertically $0\leqslant y\leqslant 1.4$. It is assumed that at $t=0$, the free surface is defined by

$$y(x,0)=1-a\sin(\pi x)$$

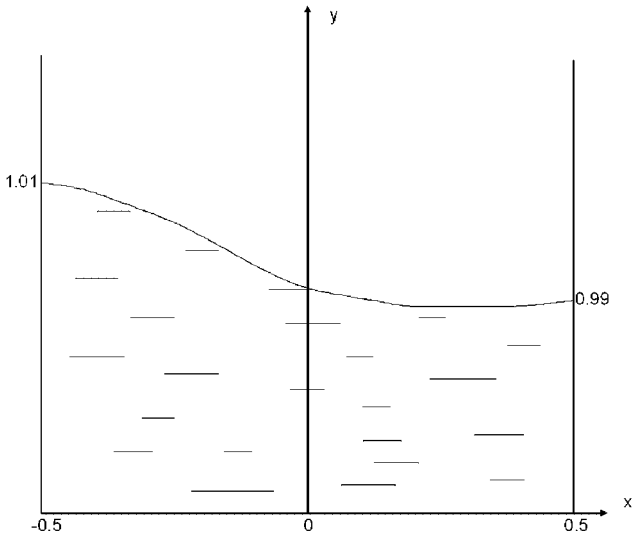

Figure 1. Sketch of wave profile at $t = 0$.

Table I. Grid resolution for different test cases.

	Grid density ($n \times m$)				Free surface region		Half band $\varepsilon = s\Delta y$
Case	$x \in (-0.5, 0.5)$	$y \in (0, \alpha)$	$y \in (\alpha, \beta)$	$y \in (\beta, 1.4)$	α	β	S
1	40	50	50	30	0.98	1.02	1.5
2	80	50	50	30	0.98	1.02	1.5
3	80	10	50	30	0.98	1.02	1.5
4	80	50	50	30	0.96	1.04	1.5
5	80	50	50	30	0.98	1.02	2.0
6	80	50	50	30	0.98	1.02	1.0/3.0

where $a = 0.01$ such that the depth of water on the left side of the tank is $h_l(-0.5, 0) = 1.01$, at the centre $h_c(-0.5, 0) = 1$ and on the right side $h_r(0.5, 0) = 0.99$. The Froude number in terms of the characteristic velocity $\sqrt{gh}$ and characteristic water depth h is $Fn = 1.0$. Figure 1 shows the sketch of free surface elevation at $t = 0$. The computational mesh consists of n uniformly spaced cells in the horizontal direction and m cells in the vertical direction. In the vicinity of the free surface $y \in (\alpha, \beta)$ the mesh consists of p uniformly spaced cells and q uniformly spaced cells above this region in air. In this computation, we use $\varepsilon = s\Delta y$ (Δy is the smallest increment near the free surface) to construct a band of finite thickness across which the fluid properties change. To illustrate the sensitivity of calculation to discretization a range of idealization models were examined as shown in Table I. The predicted values of $h_l(-0.5, t)$, $h_r(0.5, t)$ and $h_c(0.0, t)$ at $t = 3.6$ (which is approximately one period of fluid oscillation in the tank, so the value $h_l(-0.5, 3.6)$ should be close to 1.01 at this moment) as well as the

Table II. Mesh sensitivity study for different test cases (here h_l, h_r and h_c represent the depths of water on the left side, right side and at the centre of the tank).

	$h_l(t=3.6)$		$h_r(t=3.6)$		$h_c(t=3.6)$		Mass error ($t \leqslant 6.0$) (%)	
Case	Inviscid	Viscous	Inviscid	Viscous	Inviscid	Viscous	Inviscid	Viscous
1	1.00888	1.00871	0.99152	0.99166	0.99985	0.99985	0.012	0.015
2	1.00900	1.00873	0.99140	0.99165	0.99982	0.99983	0.019	0.0155
3	1.00148	1.00873	0.99847	0.99165	0.99999	0.99983	0.0145	0.0155
4	1.00946	1.00912	0.99101	0.99131	0.99979	0.99981	0.031	0.033
5	1.00897	1.00873	0.99140	0.99165	0.99982	0.99983	0.0195	0.0155
6	1.00899	1.00881	0.99140	0.99169	0.99982	0.99986	0.0195	0.0190

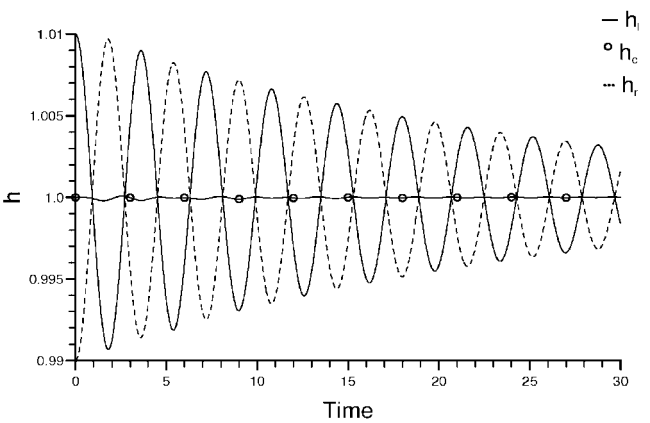

Figure 2. The time histories of free surface height on the left and right side walls of the tank and at the centre for oscillating tank problem (case 2, inviscid).

computed maximum fluid mass error at $t \leqslant 6.0$, defined by $\varepsilon_M = [M(t) - M(0)]/M(0)$, where $M(t) = \int_\Omega (1 - H(\phi))\,\mathrm{d}\Omega$, are listed in Table II for inviscid and viscous fluids ($Re = 1 \times 10^{+5}$).

The time histories of free surface height on the left and right side walls of the tank and at the centre are presented in Figure 2 for an inviscid fluid. These results show good agreement with predictions derived by Iafrati *et al.* [15]. Figure 3 shows several free surface configurations at different times.

5.2. *Broken dam problem*

Figure 4 illustrates a two-dimensional cavity of dimensions (4×2.5) in which a rectangular column of fluid of dimensions $(a \times b)$ is enclosed by a wall. The data presented relate to $a = 1$ and $b = 2$. The floor of the cavity is smooth and horizontal. At time $t = 0$, the wall is removed instantaneously and water, subject to gravity force, is free to flow along the floor. This problem was experimentally and numerically studied by Hirt and Nichols [6]. It provides a good numerical test because of the existence of both vertical and horizontal free surfaces allowing investigation of the level set method to treat surfaces which are not single valued with respect to the horizontal direction.

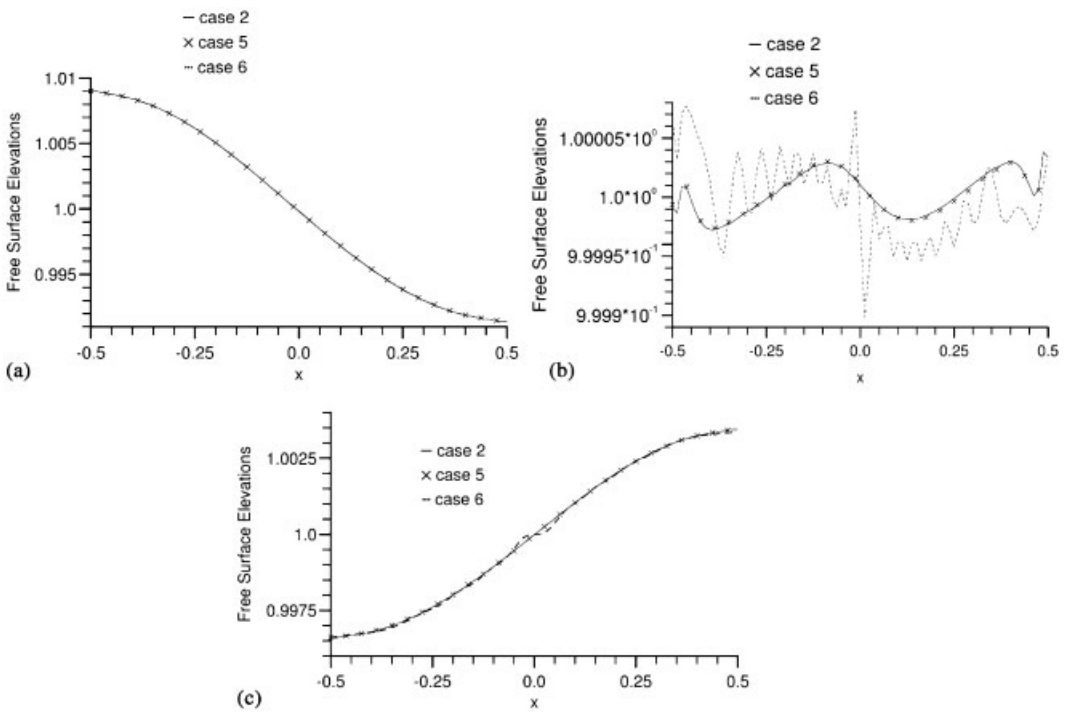

Figure 3. Free surface configurations for oscillating fluid at different times 3.6, 9.9 and 27.0 for assumed inviscid fluid: (a) time = 3.6; (b) time = 9.9; and (c) time = 27.0.

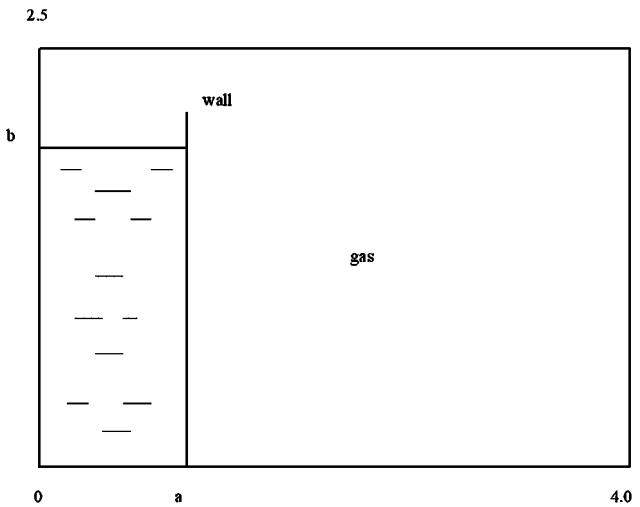

Figure 4. Cavity of two-dimensional broken dam problem.

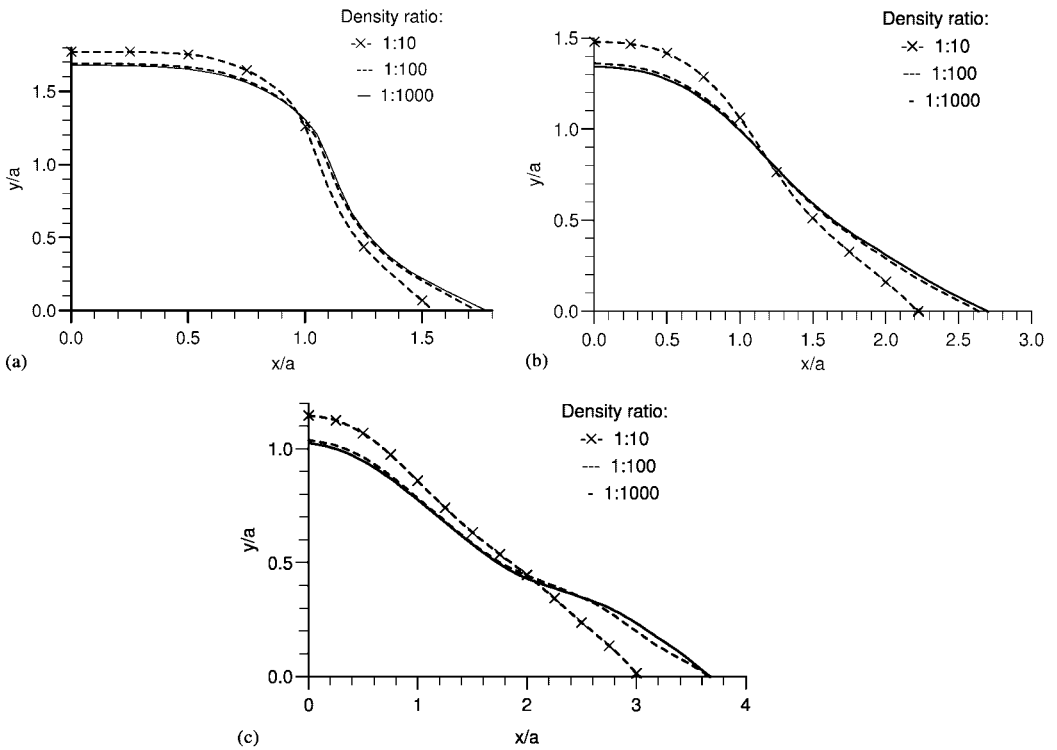

Figure 5. Free surface positions at different times 0.9, 1.4 and 1.9 for the broken dam problem ($a = 1$, $b = 2$ and water inviscid): (a) time = 0.9; (b) time = 1.4; and (c) time = 1.9.

To demonstrate the effects of gravity, different ratios of water to gas densities of 1:10, 1:100, and 1:1000 were assumed to study the water–gas interaction processes. A uniformly distributed mesh of resolution $n \times m$ was used together with a time step increment Δt and free slip boundary condition applied at the fixed boundaries. The Froude number based on the characteristic water depth b and characteristic velocity $\sqrt{gb}$ is $Fn = 1.0$. Free surface profiles at different times are presented in Figure 5 assuming the water is inviscid. The positions of the leading front of the water profile versus time in the three different density ratio cases are presented in Figure 6 and they are compared with experimental results presented by Hirt and Nichlos [6] under the condition of real fluids. The computed results show that there are only minor differences between the free surface profiles when the density ratio between the two fluids is more than 1:100. As shown in Figure 6, the comparison with the experimental data for 1:1000 is in very good agreement with theoretical prediction, but for the case 1:10 the influence of density ratio is clearly seen.

A limited sensitivity analysis involving two grids and two time-step increments were examined and the results illustrated in Figures 7 and 8 indicate only minor variation between them indicating a near convergent solution.

Numerical results were also derived after the water reaches the right-hand side wall at $x/a = 4.0$ from time $t = 0.0$ to 2.75 as shown in Figure 9(a), assuming the water inviscid, and

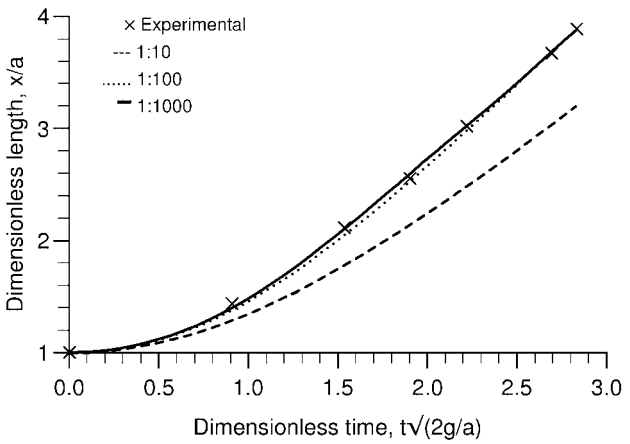

Figure 6. Comparison of calculated results of front tip position with experimental data of Hirt and Nichlos [6] for the broken dam problem (Experimental fluid: water assumed inviscid, $a = 1$, $b = 2$).

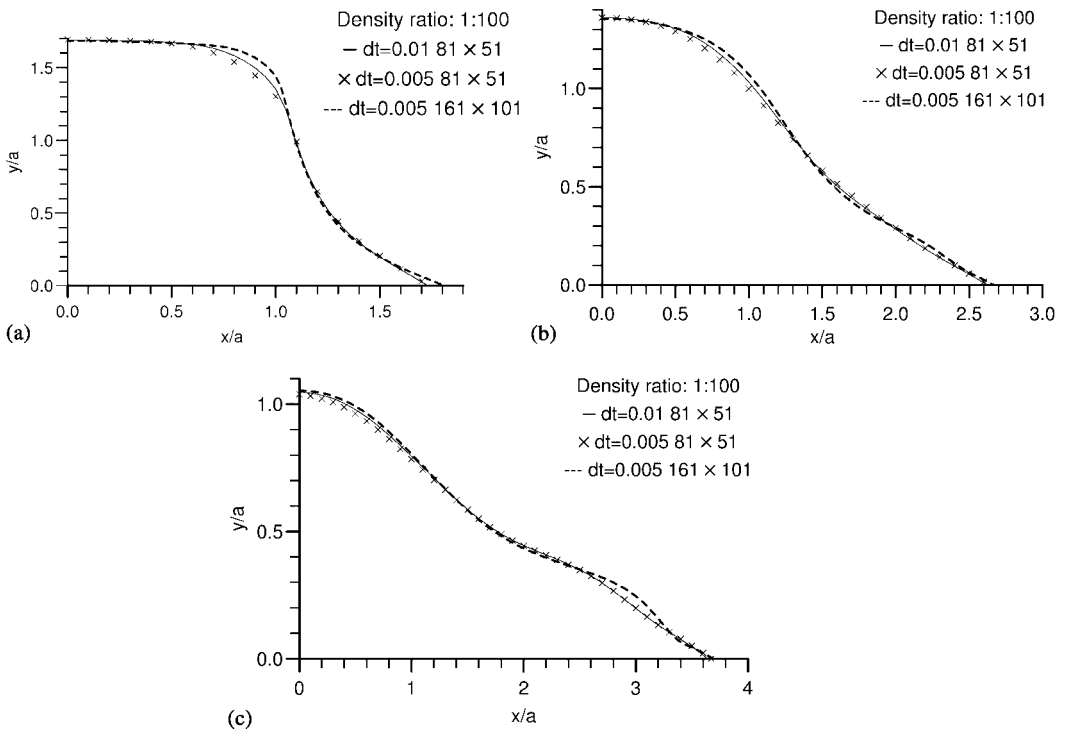

Figure 7. Effects of grid resolution and time step increment on free surface positions at different times 0.9, 1.4 and 1.9 for the broken dam problem: (a) time = 0.9; (b) time = 1.4; and (c) time = 1.9.

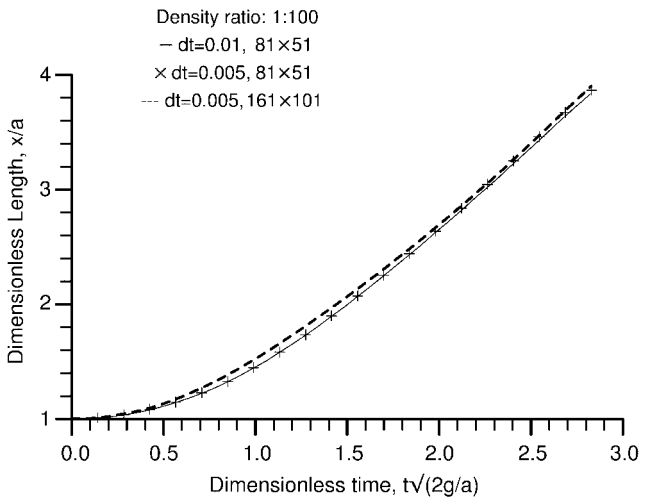

Figure 8. Comparison of the front-tip positions with different grid resolutions and time step increments for the broken dam problem.

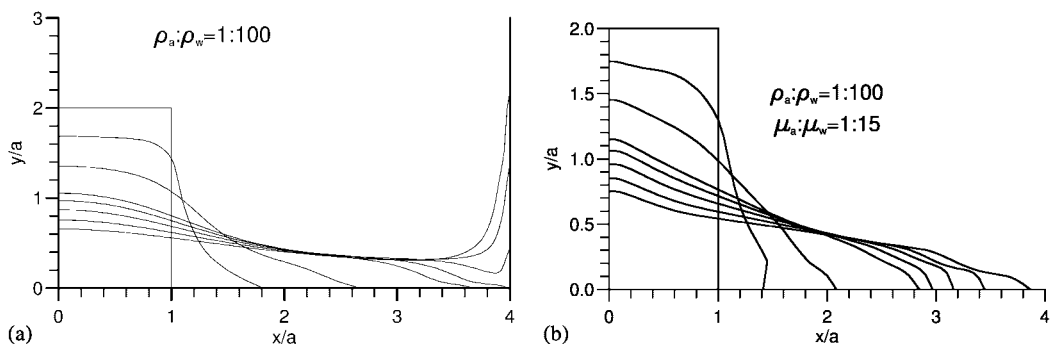

Figure 9. Evaluation of free surface shape at different times 0.0, 0.9, 1.4, 1.9, 2.05, 2.25, 2.5 and 2.75 for the broken dam problem: (a) inviscid; and (b) viscous ($Re = 100$).

Figure 9(b), treating it as viscous. The influence of viscosity is clearly seen as time increases with the inviscid fluid flowing more rapidly and interacting with the right-hand wall. This also happens with the viscid fluid but at a later time and the rise along the wall is less.

5.3. Sloshing tank problem

Sloshing free surface phenomenon is observed, for example, in fluid oscillating in a large storage tank. It may cause structural damage to the tank and if built into an aircraft, car or ship possible loss of the vehicle. Here sloshing is assessed numerically in a rectangular tank translating at different frequencies. This example further demonstrates the applicability and performance of the level set approach to capture free surface wave disturbances.

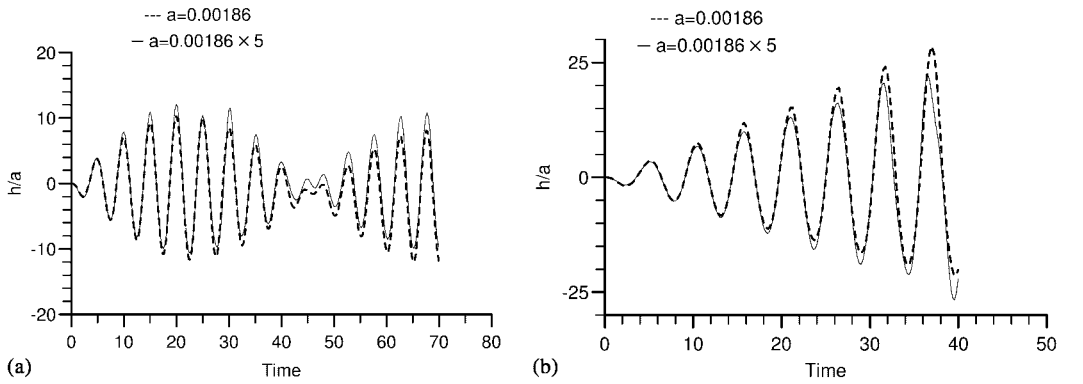

Figure 10. Time histories of free surface elevation at the left hand wall at different oscillating frequencies: (a) $\omega = 1.1\omega_0$; (b) $\omega = 0.999\omega_0$ (Fluid assumed inviscid).

A two-dimensional tank of length $L = 2$ contains water of depth $D = 1.0$ and experiences a horizontal sinusoidal displacement defined by

$$x(t) = a\sin(\omega t), \quad y = 0$$

where a denotes the amplitude of translation and ω the frequency.

Wu *et al.* [32] present the linear analytical wave elevation solution in terms of the excitation frequency ω and natural frequencies $\omega_n = \sqrt{gk_n \tanh k_n D}$ for $n = 0, 1, 2, \ldots$, where the nth wave number $k_n = (2n+1)\pi/L$ defines higher wave number components. In the latter, the wave associated with the first frequency ω_0 is dominant with the higher components contributing less to the wave elevation.

Numerical simulations were performed utilizing the proposed algorithm for horizontal displacements of small amplitude $a = 0.00186$ and a relatively larger amplitude $a = 5 \times 0.00186$ together with two excitation frequencies $\omega = 1.1\omega_0$ and $\omega = 0.999\omega_0$ which lie very close to the natural frequency ω_0. Froude number $Fn = 1$ is defined by the characteristic velocity $\sqrt{gD}$ for the characteristic water depth D and a free slip boundary condition is applied on the three walls. The water was treated as inviscid.

Figure 10 shows the time histories of free surface wave elevation at the left-hand side of the tank ($x = -L/2$) at different frequencies and different amplitudes. It is seen from Figure 10(b) that the wave amplitude increases with time. This is due to the small difference $\Delta\omega = |\omega - \omega_0|$ between the excitation frequency ω and the natural frequency ω_0 producing a very large envelope period of the amplitude-modulated wave $2\pi/\Delta\omega$. The amplitude of wave at the left-hand side wall does not, of course, tend to infinity with time and nonlinear phenomena (excluding breaking waves) are retained in the numerical simulation.

Further exploratory calculations of the fluid sloshing phenomenon in a partially filled two-dimensional tank showed that there are no obvious differences observed in the time histories of free surface wave elevation at the left-hand side of the tank when parameter ε is set to $0.5\Delta y$, $1.0\Delta y$ and $1.5\Delta y$, respectively, where Δy denotes the vertical distance between two grid points. Numerical experiments allowing water to move upwards and to hit the top

boundary of a closed container subject to translational harmonic motion indicate that the peak value of the impact pressure depends strongly on the value of the half thickness of interface ε assumed in the mathematical model.

5.4. Flow around a Wigley ship hull

5.4.1. Computational conditions and grids for three chosen test cases. The simulation of free surface waves generated by a three-dimensional Wigley form [33] moving in calm water introduces far field inflow and outflow boundaries into the numerical process analysing the hull–viscous fluid interaction.

The Wigley hull of maximum beam B, length L and draught D is defined by a rectangular side elevation, and a parabolic profile for the beam both in length and in draught. The beam of the hull is defined by the analytical expression

$$y = \frac{B}{2}\left(1 - \left(\frac{2x}{L}\right)^2\right)\left(1 - \left(\frac{z}{D}\right)^2\right) \tag{37}$$

In the numerical calculations, a hull with ratio $L : B : D = 1 : \frac{1}{10} : \frac{1}{16}$ is used to simulate the free surface flow.

Since this hull form is port-starboard symmetric only one-half is needed in the computation. For this sharp-keeled body three H-type grids were generated for a computational domain extending in the lengthwise direction from $x = -1.5L$ to $2.5L$. Clustering is used near the bow and the stern in the ξ-direction (longitudinal direction), near the hull surface in the η-direction (radial direction), and near the free surface in the ζ-direction (girth direction). The mesh is generated using a simple algebraic method. That is, at each section, the circumferential lines comprise of parabolae similar to the hull profile where the maximum values of beam and draught defining the outside boundary are both equal to unity. The computational domain is extended to half draft above the mean free surface. Table III presents the three grid levels, with a grid refinement ratio of $\sqrt{2}$ ($r = \sqrt{2}$), used in the computations and the total number of discretized elements in the finest mesh is about half a million.

All variables are non-dimensional in terms of ship length L, the free-stream velocity U_0 and the water density ρ_w. In terms of these characteristic variables the drag coefficients are non-dimensionalized by $\frac{1}{2}\rho_w U_0^2 L^2$. Flows are calculated for three different test cases: (i) $Fn = 0.25$, $Re = 3.7 \times 10^{+6}$, (ii) $Fn = 0.316$, $Re = 4.6 \times 10^{+6}$ and (iii) $Fn = 0.35$, $Re = 5.1 \times 10^{+6}$, respectively. The ship hull is fixed in space and not allowed to trim.

Table III. Computational grid for three test cases involving Wigley ship hull.

	Resolution	Before bow $(-1.5L, -0.5L)$	Between hull $(-0.5L, 0.5L)$	After stern $(0.5L, 2.5L)$	Below mean free surface $(-1.0D, 0)$	Above mean free surface $(0, 0.5D)$
Grid-1	$78 \times 25 \times 33$	15	36	27	18	15
Grid-2	$110 \times 35 \times 46$	21	50	39	25	21
Grid-3	$156 \times 50 \times 65$	30	70	56	35	30

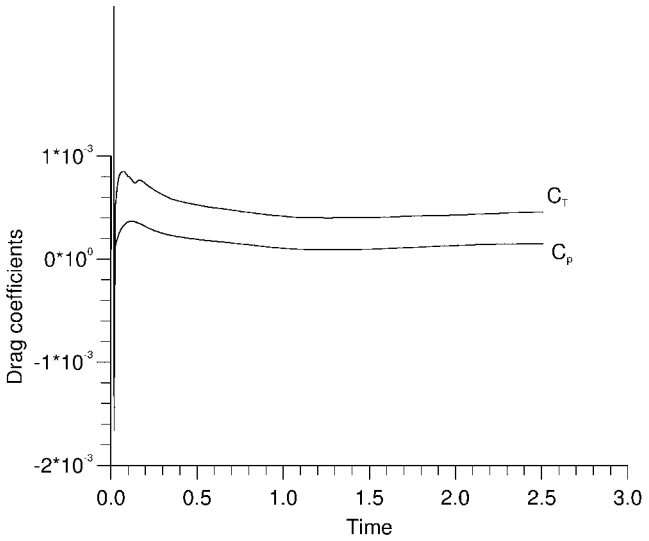

Figure 11. History of the drag coefficients for the medium grid density described in Table IV; ($Fn = 0.316, Re = 4.6 \times 10^{+6}$) C_T: total drag, C_P: pressure drag.

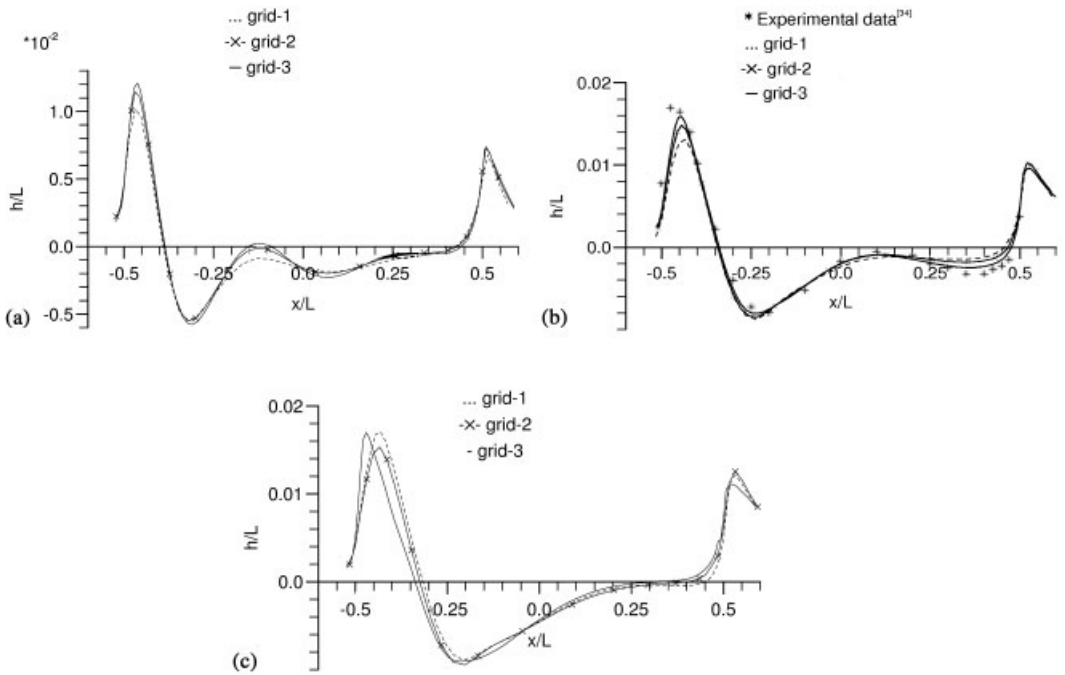

Figure 12. Wave profiles along the hull surface at different Froude numbers and different grid levels: (a) $Fn = 0.25$, $Re = 3.7 \times 10^{+6}$; (b) $Fn = 0.316$, $Re = 4.6 \times 10^{+6}$; (c) $Fn = 0.35$, $Re = 5.1 \times 10^{+6}$.

Table IV. Comparison of calculated drag coefficient and experimental data C_T: total drag coefficient, C_P: pressure drag coefficient.

Conditions	Drag coefficients ($\times 10^{+3}$)	Grid-1 (coarse)	Grid-2 (medium)	Grid-3 (finest)	Experimental Data [35]
$Fn = 0.25$	C_T	4.91	4.91	4.82	4.57
$Re = 3.7 \times 10^{+6}$	C_P	0.918	1.03	1.09	0.77
$Fn = 0.316$	C_T	5.45	5.64	5.67	5.11
$Re = 4.6 \times 10^{+6}$	C_P	1.42	1.58	1.68	1.51
$Fn = 0.35$	C_T	5.39	5.75	5.94	5.0
$Re = 5.11 \times 10^{+6}$	C_P	1.55	1.65	1.58	—

5.4.2. Calculated results for three grid levels and three Froude numbers. Figure 11 displays the convergence history of the total resistance coefficient C_T and pressure resistance coefficient C_P at Froude number $Fn = 0.316$ for the medium grid density. The wave profiles along the hull computed using the three grid levels and for different Froude numbers are shown in Figure 12. It can be seen from Figure 12(b) that the grid with the finest resolution (grid-3) gives the best agreement compared with experimental data [34]. In Figure 12(c), significant differences arise between the wave profiles calculated using the finest grid and the other two grids. These results suggest that to provide better agreement with experimental data more refined resolutions are required increasing computational effort and time. However, the approach described herein shows merit and with refinement of the numerical scheme of study it is expected that improved agreement will arise.

Finally, estimated resistance coefficients are presented in Table IV for the different discretization schemes. All coefficients are non-dimensional in terms of $\frac{1}{2}\rho_w U_0^2 S$, where S represents the wetted surface area of the Wigley ship hull.

6. CONCLUSIONS

In this study we applied a level set formulation in generalized curvilinear coordinates to viscous flows characterized by a moving free surface. To illustrate the numerical approach fluid–structure interaction problems associated with an oscillating flow, a dam failure, sloshing and a ship wave generated by a translating Wigley hull were chosen to validate the numerical algorithm by adopting several computational grids and/or different time step increments. The proposed method was verified through a limited comparison with independent findings. The present approach to the two types of free surface flows relating to internal and external flow modelling requires further validation against more comprehensive experimental studies. The analysis requires extension to include studies of pressure loads when the water reaches the right-hand side wall of the dam failure problem and impact loadings in the sloshing problem for different depths of water treated as inviscid or viscous. With modifications the present method has the potential to simulate complicated free surface problems frequently arising in fluid–structure interaction problems involving, for example, overturning, breaking, merging and reconnected waves as well as treating the structure as a three-dimensional flexible body.

ACKNOWLEDGEMENTS

Dr Y. G. Chen is grateful for the funding of this investigation from the Lloyd's Register University Technology Centre, School of Engineering Sciences.

REFERENCES

1. Watanake O, Masuko A, Shiorose Y. Numerical simulation of a wave-viscous flow about a ship including propeller effects. *Twentieth Symposium on Naval Hydrodynamics* 1994; 85–97.
2. Takai M, Zhu M. Finite-volume simulation of viscous flow about ship with free-surface by Arbitrary-Lagrange–Euler method. *Proceedings of CFD Workshop*, Tokyo, 1994; 85–94.
3. Harlow FH, Welch JE. Numerical calculation of time-dependent viscous incompressible flow of fluid with free surface. *Physics of Fluids* 1965; **8**:2182–2189.
4. Suzuki A, Miyata H, Kajitani H. Numerical analysis of free surface shock waves around a bow by modified MAC-method (First Report). *Journal of Society of Naval Architects of Japan* 1981; **150**:1–8.
5. Miyata H, Zhu M, Watanabe O. Numerical study of a viscous flow with free-surface waves about a ship in steady straight course by a finite-volume method. *Journal of Ship Research* 1992; **36**:332–345.
6. Hirt CW, Nichols BD. Volume of fluid (VOF) method for the dynamics of free boundaries. *Journal of Computational Physics* 1981; **39**:201–225.
7. McKibben JF, Aidun CK. Extension of the volume-of-fluid method for analysis of free surface viscous flow in an ideal gas. *International Journal for Numerical Methods in Fluids* 1995; **21**:1153–1170.
8. Maronnier V, Picasso M, Rappaz J. Numerical simulation of free surface flows. *Journal of Computational Physics* 1999; **155**:439–455.
9. Shin S, Lee W. Finite element analysis of incompressible viscous flow with moving free surface by selective volume of fluid method. *International Journal of Heat and Fluid Flow* 2000; **21**:197–206.
10. Osher O, Sethian JA. Fronts propagating with curvature-dependent-speed: algorithms based on Hamilton–Jacobi formulations. *Journal of Computational Physics* 1988; **79**:12–49.
11. Sethian JA, Strain J. Crystal-growth and dendritic solidification. *Journal of Computational Physics* 1992; **98**:231–253.
12. Sussman M, Smareka P, Osher S. A level set approach for computing incompressible two-phase flows. *Journal of Computational Physics* 1994; **114**:146–159.
13. Chang YC, Hou TY, Merriman B, Osher S. A level set formulation of Eulerian interface capturing methods for incompressible fluid flows. *Journal of Computational Physics* 1996; **124**:449–464.
14. Zhang H, Zheng LL, Prasad V, Hou TY. Curvilinear level set formulation for highly deformable free surface problems with application to solidification. *Numerical Heat Transfer*, *Part B*: *Fundamentals* 1998; **34**(1):1–20.
15. Iafrati A, Di Mascio A, Campana EF. A level set technique applied to unsteady free surface flows. *International Journal for Numerical Methods in Fluids* 2001; **35**:281–297.
16. Yue W, Lin C, Virendra CP. Numerical simulation of unsteady multidimensional free surface motions by level set method. *International Journal for Numerical Methods in Fluids* 2003; **42**:853–884.
17. Sussman M, Dommermuth D. The numerical simulation of ship waves using cartesian grid methods. *Twenty third Symposium on Naval Hydrodynamics* 2001; 762–779.
18. Mascio D, Muscari R, Broglia R. Computation of free surface flows around ship hulls by a level-set approach. *The Eighth International Conference on Numerical Ship Hydrodynamics*, Busan, Korea, September 22–25, 2003.
19. Baldwin BS, Barth TJ. A one-equation turbulence transport model for high Reynolds number wall bounded flows. *29th Aerospace Sciences Meeting*, Reno, Neveda, 1991.
20. Ferziger JH, Peric M. *Computational Methods for Fluid Dynamics* (3rd edn). Springer: New York, 2002.
21. Chorin AJ. A numerical method for solving incompressible viscous flow problems. *Journal of Computational Physics* 1967; **2**:12–26.
22. Rogers SE, Kwak D. Upwind differencing scheme for the time-accurate incompressible Navier–Stokes equations. *AIAA Journal* 1990; **28**(2):253–262.
23. Roe PL. Approximate Riemann solvers, parameter vectors and difference schemes. *Journal of Computational Physics* 1981; **43**:357–372.
24. Rogers SE, Kwak D. An upwind differencing scheme for the steady-state incompressible Navier–Stokes equations. *Applied Numerical Mathematics* 1991; **8**(1):43–64.
25. Kelecy FJ, Pletcher RH. The development of a free surface capturing approach for multidimensional free surface flows in closed containers. *Journal of Computational Physics* 1997; **138**:939–980.
26. Toro EF. *Riemann Solvers and Numerical Methods for Fluid Dynamics—A Practical Introduction* (2nd edn). Springer: New York, 1999.

27. Barth TJ. Analysis of implicit local linearization techniques for upwind and TVD algorithms. *AIAA Paper* 87-0595, 1987.
28. Peng D, Merriman B, Osher S, Zhao H, Kang M. A PDE-based fast local level set method. *Journal of Computational Physics* 1999; **155**:410–438.
29. Harten A, Engquist B, Osher S, Chakravarthy SR. Uniformly high order accurate essentially non-oscillatory schemes III. *Journal of Computational Physics* 1986; **71**:231–303.
30. Osher S, Shu CW. High-order essentially non-oscillatory schemes for Hamilton–Jacobi equations. *SIAM Journal on Numerical Analysis* 1991; **28**(4):907–922.
31. Gloth O, Hanel D, Tran L, Vilsmeier R. A front tracking method on unstructured grids. *Computers and Fluids* 2003; **32**:547–570.
32. Wu GX, Ma QW, Taylor RE. Numerical simulation of sloshing waves in a 3D tank based on a finite element method. *Applied Ocean Research* 1998; **20**:337–355.
33. Baar JJM. A three-dimensional linear analysis of steady ship motion in deep water. *Ph.D. Thesis*, Brunel University, 1986.
34. Cooperative experiments on Wigley parabolic models in Japan. *Seventieth ITTC Resistance Committee Report*, 1983.
35. Ju S. Study of total and viscous resistance for the Wigley parabolic ship form. *IIHR. Report No. 261*, Iowa Institute of Hydraulic Research, University of Iowa, Iowa City, Iowa, 1983.

